Am J Transl Res 2022;14(4):2527-2539
www.ajtr.org /ISSN:1943-8141/AJTR0138473

Original Article

Cranio-maxillofacial post-operative face prediction by deep spatial multiband VGG-NET CNN

Rizwan Ali[1], Rui Lei[1], Haifei Shi[2], Jinghong Xu[1]

Departments of [1]Plastic Surgery, [2]Orthopedics, The First Affiliated Hospital, School of Medicine, Zhejiang University, No. 79 Qingchun Road, Hangzhou 310003, Zhejiang, China

Received August 22, 2021; Accepted October 25, 2021; Epub April 15, 2022; Published April 30, 2022

Abstract: Current plastic and reconstructive surgery computational techniques are not precise and take a long time to perform. Therefore, these limitations reduced the adoption of computational techniques. Although computer-aided surgical preparation systems may help to enhance clinical results, minimize operating time and costs, they are too complicated and require detailed manual information, which restricts their usage in doctor-patient communication and clinical decision-making. In order to obtain the optimal aesthetic and reconstruction treatment results, these techniques must be designed and implemented carefully. Computer-aided modeling, planning, and simulation techniques enable the preoperational evaluation of various therapeutic strategies based on the 3D patient models. We offer the new deep-learning architecture for diagnostics, risk stratification, and post-operative simulation for face prediction. Initially, preprocessing was done by using the weighted adaptive median filter and Laplacian partial differential equation-based histogram equalization. Then the target area was converted to 3D for clear visualization by using the Smart restorative frustum model. Finally, the post-operative face prediction was constructed by using the deep spatial Multiband VGG NET CNN. We obtained a face dataset of 313,318 CT and their clinical records from different centers. The algorithms were developed by 21,095 scans (Qure25k data set). In addition, CQ500 datasets from various centers were compiled in two batches, B1 and B2, to validate the algorithms clinically. Four hundred ninety-one scans used the CQ500 dataset. Initially, we reconstructed the input image and then devised the post-operative face computationally. The suggested deep spatial Multiband VGG NET CNN showed the high range of post-operative face prediction accuracy. Therefore, successful metrics such as the Jaccard and dice scores have shown accurate outcomes compared to other traditional methods. MATLAB was used to obtain the output of proposed work. With the help of the suggested classifier, the prediction accuracy was 93.7%, sensitivity was 99.9%, and specificity was 99.8%, all of which were higher than traditional approaches. Here, the suggested method provides better results for post-operative face prediction to the applied dataset than any other existing mechanisms. It is a generalized attempt that can apply to other similar datasets as well.

Keywords: Plastic and reconstructive surgery, surgical planning, post-operative face prediction, weighted adaptive median filter, histogram equalization, smart restorative frustum model, deep spatial multiband VGG NET CNN

Introduction

Every year, in the United States, more than 200,000 maxillofacial treatments are performed for various infections, illnesses, and injuries to the face, neck, and head. A significant amount of patient detail is gathered to create and automate customized methods in machine learning-based applications for these operations. The machine learning surgical techniques are relatively new in plastic and reconstructive surgery. It has been utilized to illustrate how it can alter skull-development syndrome and how the remedial effects of surgery on skull deformities can be examined or predicted. Preoperative work includes medical imaging and computer-assisted surgical preparation. Evaluating various operating options in a simulated world would save operational time, costs and promote a more consistent and optimal treatment. To determinate the right bone cuts and bone orientation, a surgeon can manipulate a digital patient model reconstructed with CT or MR images and reproduce face shape shifts. This immersive treatment procedure can be used for patients to produce tai-

lored wafers, cutting aids, plates, and implants. Though 3D computer-aided operational planning has existed for 30 years and the advantages of conventional 2D planning are recognized, its adoption has been restricted to high-quality hospitals, primarily because of the complexities of business software and disputed planning precision. Deep learning models, including predictive types, were proposed to make this technology available and simplify the processes in computer-assisted operational planning. However, incorrect face modeling challenges have been considered the vast anatomical diversity of human populations. A wide variety of 3D images from diverse populations ages, sexes, and ethnicities are needed to develop a mathematical model which can correctly represent an individual face. These 3D photos have to be processed by the new computer vision algorithms and instantly create an elevated mathematical model. In the beginning, a popular approach to deep learning was used to retrieve accurate and complete 3D images for 2D images and simulate statistic models for the face and texture. Presently, deep learning techniques are used to identify the face, standardize expressions, and recreate the video for the face. Therefore, we suggest a deep-learning system with various factors, completely integrated diagnostic and clinical decision-making processes in the field of craniomaxillofacial surgery. The full-automation-wide clinical model is available for diagnosis, risk stratification, and simulation of therapy. We also trained and validated a proposed deep spatial Multiband VGG NET CNN based on 313,318 head CT scans of healthy volunteers and patients receiving craniomaxillofacial surgery. CNN showed clinical decision-making potential, including a fully automatic diagnostic and simulation procedure. Our proposed model is crucial in making the surgical procedure easy for surgeons, inexpensive, and more transparent to patients based on the machine. It would turn patients into unique systems of orthography therapeutic decision-making and other plastic and reconstructive surgical areas. The remaining part of the paper can be arranged as follows; Section II represents different methods used so far. The problem statement is illustrated in section III. The full description of the procedure proposed is given in section IV. The analytical aspect of the suggested scheme is section V. The overall workflow will eventually end in section VI.

Related works

Machine learning, a branch of artificial intelligence, can tackle clinically related problems in several fields of plastic surgery [1]. Even in difficult circumstances, advanced imaging tools such as computer-assisted surgery (CAS) can help with preoperative planning. Device placement and the shape of complex osteotomies can both be adjusted intra-operatively. Postoperative monitoring and long-term follow-up are both possible with CAS [2]. Furthermore, in craniomaxillofacial (CMF) surgery, selecting the right surgical plan is critical to obtaining the desired aesthetic facial profile [3]. In the research of Shahim et al. [3], the predicted plan for osteotomy of 6 clinical cases that undergoes CMF surgery was compared to the actual clinical plan. After that, the predicted and actual clinical plans were used to compare simulated soft-tissue results. The comparison of both facial outlook and the strategy for osteotomy indicates a high level of agreement, indicating that the suggested technique might be used in the prediction of CMF surgical planning. In the research of Okamoto et al. [4], the goal of his study was to assess 3D hard and soft tissues changes following mandibular setback surgery between orthodontics-firt approach (OFA) and surgery-first approach (SFA). Okamoto et al. discovered that soft tissue changes following the SFA differed significantly from those after the OFA; hence, soft tissue predictions need additional care. An analysis of data comparing SFA and OFA for patients with mandibular prognathic confirms that post-operative orthodontic therapy and occlusal relationship in SFA modify the mandibular soft tissue. Bianchi et al. [5] performed a cone-beam computed tomography (CBCT) pre-operatively on 10 patients with CMF deformations. The data were recreated in three dimensions by using the SurgiCase CMF software, and several osteotomies were simulated in a 3D virtual environment by employing dissimilar surgical methods. After six months of surgery, the patients received another CBCT. As a result, the pre- and post-operative CBCT investigations may be superimposed to assess the software's consistency and dependability. The preliminary findings of this study showed that in addition to the minimal radiation exposure, CBCT-based simulations in orthognathic surgery for CMF abnormalities are trustworthy, and might become the gold standard for surgi-

cal treatment planning. Fiducial markers, such as titanium spheres, ceramic balls, softened gutta-percha, acrylic, or face-bow, were used in the methods of Gateno et al. [6], Uechi et al. [7], and Nairn et al. [8] to create a proper procedure of replacing the contorted dental image without accounting for faulty imaging effects obtained by CBCT. In the research of Steinbacher et al. [9], 3D analysis and common threads of all six forms of reconstruction (cranial reconstruction, craniosynostosis, midface advancement, mandibular distraction, mandibular reconstruction, and orthognathic surgery) are emphasized and compared to novel CMF surgical applications. According to the findings of this study, 3D planning and virtual surgery improve efficiency, specificity, originality, and repeatability in CMF surgery. Bauermeister et al. [10] presented a literature review study on 3D printing technology concerning plastic and reconstructive surgery. This study concluded that 3D printing allows for the formation of complex customized implants which enhance patient outcomes and the economic viability of the procedure. This technology provides a degree of accessibility for distant and resource-constrained areas where health care is typically scarce. In the investigation of Bhalodia et al. [11], the Shape Works software was used to analyze the form of the skull. Combining researcher evaluations with their shape analysis model, machine learning was utilized to anticipate the intensity of metopic craniosynostosis (CS) using CT scans. Interfrontal angles then contrasted their model with the gold standard. This technique may make it easier for physicians to measure the intensity of the illness and conduct comprehensive longitudinal examinations. Jalali et al. [12] developed an algorithm for machine learning to predict the required blood transfusion in human craniofacial surgery preoperatively. Plastic surgeons can use this prediction model to enhance the clinical care of patients presenting for CS surgery. Brucoli et al. [13] conducted a study to evaluate and explain experience by using a teleradiology approach on facial trauma patients. Telemedicine systems handled 467 patients with a total of 650 fractures. According to findings, teleradiology may be useful in properly triaging trauma patients from outlying hospitals for the correct referral to a maxillofacial trauma hub center. Van de Lande et al. [14] proposed combined machine learning and geometric morphometrics model to allocate detailed and precise facial shapes. Their implementation seems to be highly useful in surgical preparation and evaluation. However, a clinical tool must also be developed to use this model. Miller et al. [15] compared the eFACE scale of a clinician to the automated evaluations of machine-learning (auto-eFACE). According to their findings, auto-eFACE is a rapid and simple evaluation method that can standardize facial palsy outcome metrics and reduce observer bias found in eFACE clinician scales. Tonutti et al. [16] proposed a procedure to evaluate a brain deformation paradigm for patients by integrating data from the finite element method (FEM) and learning algorithms. The results outperform previous deformation models for real-time applications, with lower errors and higher patient specificity. The suggested method satisfies the present demands of image-guided surgical techniques and can simulate any soft tissue deformation. Stepanek et al. [17] used the R programming language to do multivariate regression to find factors that increase face attractiveness following rhinoplasty. Based on the Ekman-Friesen FACS scale, Bayesian Naive Classificatory, neural networks and decision trees (CART) were used to allocate facial image data to one of the facial emotions. In this research, performed machine learning analysis showed the highest accuracy and increased facial attractiveness. Mostoufi et al. [18] demonstrated that digital technology has transformed the landscape of maxillofacial surgery, particularly orthognathic techniques, and it is continually evolving. As a result, clinicians must be aware of and understand available alternatives while keeping abreast of these developments. It illustrates the impact of advanced technology in orthognathic surgery by explaining the fundamental principle of virtual planning and navigation with examples of surgical procedures. Gerbino et al. [19] assessed 3D soft tissue and bone alterations in the malar region by using malar valgisation osteotomy combined with orthognathic surgery. In midface hypoplasia, malar valgisation osteotomy combined with orthognathic surgery improved the zygomatic projection and contributes to a balanced facial correction. A volume and surface analysis based on 3D geometrical data showed enhancement in the transversal and forward directions. Thus, the osteotomy can be done safely, when combined with orthognathic

procedures. Hemelen et al. [20] proposed a study to compare the prediction accuracy of a conventional 2D planning with a 3D computer-aided planning in hard and soft tissue profiles. The 3D planning method allows for more precise soft tissue planning. Nevertheless, the 2D orthognathic planning is equivalent to 3D planning when it comes to hard tissue planning. In the research of Hertanto et al. [21], the study's main goal was to investigate patients' perceptions about the influence of 3D prediction planning (3D PP) of facial soft tissue changes after orthognathic surgery. The 3D PP had a noteworthy positive impact on the patients' experience of their orthognathic management journey. Its improved surgeon-patient communication while reducing patients' preoperative anxiety and increasing their motivation and confidence to undertake surgery. The 3D PP was accurate and did not overestimate the expected changes.

Problem statement

Corrective procedure for congenital abnormalities and organ transplantation cells for a rigorous preparatory process during which many studies are performed. It could be dangerous without an accurate knowledge of the relationship and the structure involved in an operation. Thus, an appropriate configuration is required to schedule surgical procedures correctly.

Proposed methodology

The benefits of preoperative imaging include the opportunity to test potential treatments, e.g., different points of entry, access points, pathways, sites, and collection of implants by the surgical instruments. It also enables the surgery to be more precise, durable and reduces complications. Preoperative preparation based on images aims to identify a viable solution in challenging situations and facilitates patient access to surgery. The schematic representation of the suggested methodology is depicted in **Figure 1**.

Pre-processing

Pre-processing was the first phase of image processing. Pre-processing ensured the compatibility and performance of the database. Each step was required to reduce the workload of image processing. Filtering and extracting methods identified the unintentional errors that impaired the image's capacity and were used for pretreatment. Pre-processing was done to enhance the contrast of the images. The first weighted adaptive median filter stopped other unexpected sounds from occurring. Thus, the noise was eliminated to produce a translucent image.

$$\hat{\sigma}^2{}_i = \frac{1}{I - b - 1} \sum_{j=1_{j\neq 1}}^{n} \in^2{}_j \tag{1}$$

Where b, d is the parameter, and σ represents standard deviation. Following that, the errors should be independent of one another, and it can be described as follows,

$$S_i \sim \sqrt{o} \frac{T}{\sqrt{t^2 + o - 1}} \tag{2}$$

Where S represents a random variable. Then the movement of the variable needs to be normalized by the standard deviation.

$$D = \frac{\mu^v}{o^v} \tag{3}$$

Where D denotes the moment scale.

$$\mu^k = F(P-\mu)\hat{}K \tag{4}$$

Where P is a random variable and F is the expected value.

$$o^k = \sqrt{(F(P - \mu)\hat{}v)\hat{}2} \tag{5}$$

For normalizing the distribution of the variable using the mean.

$$C_v = \frac{f}{\overline{P}} \tag{6}$$

Where C_v is the co-efficient of the variance.

The improved pixels in this step were converted into binary images by an automatic threshold mechanism. It was achieved by establishing whether each pixel was a vessel pixel (value 1) or a background pixel threshold (value 0). This approach was more accurate than the standard threshold technology. The threshold utility was automatically determined by a standard intra-class variance global threshold measurement procedure. Isolate image threshold artifacts or some other related digital image information. During the thresholding process, warped pixels usually produce error pixels. The scaling function can do by setting the values between 0 and 1. This technique is called stan-

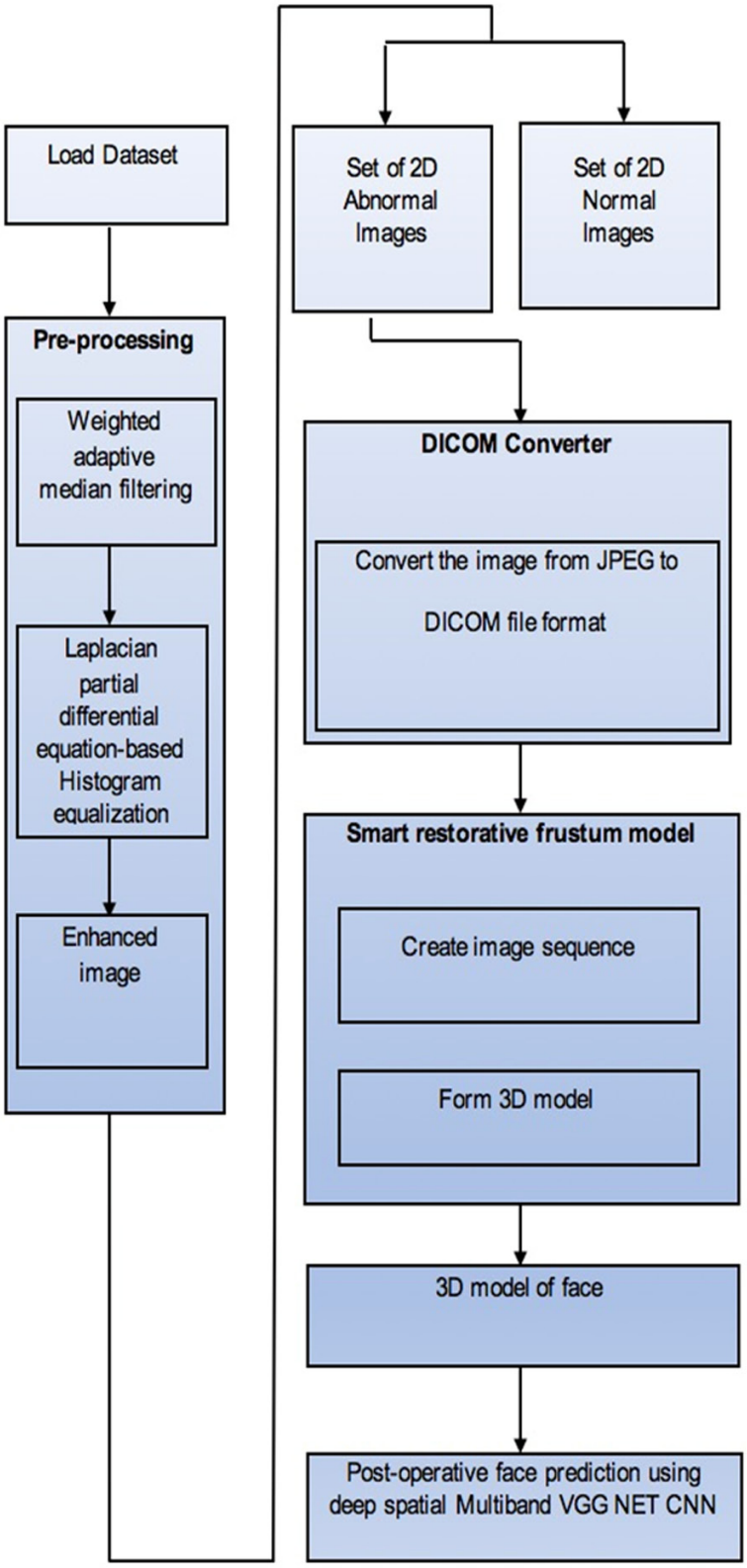

Figure 1. Flow diagram of the proposed methodology.

dardization, depending on the application, and it reduced the noise perfectly.

$$P' = \frac{(P - P_{min})}{(P_{max} - P_{min})} \quad (7)$$

Afterwards, in general, the histogram equalization can be done to boost the contrast. Since the histogram was equalized, the average contrast of the images was then improved. However, the partially difference-oriented Laplacian model may be proposed for improving the irregular pixels. The use of the RGB space was much convenient since it can take images from any capturing source without transformation any of the light images. Consequently, the RGB space was extensively used in current working systems and also in the process of image processing. **Figure 2** shows the pixel color representation.

$$X = \frac{X}{R_r, G_g, B_b} \quad (8)$$

$$Y = \frac{Y}{R_r, G_g, B_b} \quad (9)$$

$$Z = \frac{Z}{R_r, G_g, B_b} \quad (10)$$

Here, $R_r+G_g+B_b=1$

Where X denotes red intensity, Y denotes green intensity, and Z denotes blue intensity.

The algorithm is then rewritten as a partial variance equation,

$$ØE(R_r,G_g,B_b)/,t=F(R_r,G_g,B_b)-E(R_r,G_g,B_b) \quad (11)$$

Where $E(R_r,G_g,B_b)$ represents the continuous pixel while $F(R_r,G_g,B_b) = f\{E(R_r,G_g,B_b)\}V = FINT\{E(R_r,G_g,B_b)\}$ and the following expression can be found by using the finite difference method.

$$E^{t+1}(X,Y) = E^t(X,Y) + [\{E(R_r,G_g,B_b) - E(R_r,G_g,B_b)\} V\Delta t] \quad (12)$$

By scaling the noise, we can smooth the pixel in this process. Thus, by applying the anisotropic diffusion formula, a transformed expression will,

$$\emptyset E(R_r,G_g,B_b)/\emptyset t=\mu c_{RN}(\|\nabla E(R_r,G_g,B_b)\|)\mathrm{div}(\nabla E(R_r,G_g,B_b)/\|\nabla E(R_r,G_g,B_b)\|) + f(R_r,G_g,B_b) - E(R_r,G_g,B_b) \quad (13)$$

Where μ represents the weighing factor that maintains the smoothing process, $\nabla S(X,Y,Z)$ was the gradient of the pixel, c_{CRN} was the diffusion coefficient.

$$C_{RN}=\|\nabla E(R_r,G_g,B_b)\|=1/1 + [\|\nabla E(R_r,G_g,B_b)\|/k]^2 \quad (14)$$

The expression β has a higher smoothing value for the equation smoothing, but pixels must be reinforced before smoothing. However, a linear pixel amplification operator such as Laplacian has sharpened and masked the pixel. We want to selectively sharpen the pixels to stabilize the environment and to prevent noise from enhancing. The method of forwarding and backward diffusion can apply according to Laplacian as,

$$c_{FBD}(\|\nabla E(R_r,G_g,B_b)\|=1/1+[\|\nabla E(R_r,G_g,B_b)\|/f_k]^n\alpha/1+\|\nabla E(R_r,G_g,B_b)\|f_k)\vartheta]^2m \quad (15)$$

The FAB approach was inappropriate for texture safety and was ideal for pixel fluidity. The smoothing must then continue with a reasonable sharpening rate without changing the pixel. Therefore, we have changed the equation for the new expression Laplacian:

$$\phi E(R_r, G_g, B_b)/, t = \mu c_{FBD}(\|\nabla E(R_r, G_g, B_b)\| \mathrm{div} \frac{\nabla E(R_r, G_g, B_b)}{\|\nabla E(R_r, G_g, B_b)\|} + [f(R_r, G_g, B_b) - (R_r, G_g, B_b)] - \mu \triangle \hat{} 2\, E(R_r, G_g, B_b) \quad (16)$$

It leads to the generally accepted PDE formulation and improved continuous initial image field E (R, G, B) in the form of smoothing/sharpening,

$$\emptyset S(R_r,G_g,B_b)/\emptyset t=\mu\, g_{FBD}(S(R_r,G_g,B_b)) + g_e(S(R_r,G_g,B_b)) + \mu g_e(S(R_r,G_g,B_b)) \quad (17)$$

Where $g_{FBD}(S(R_r,G_g,B_b))$, $g_e(S(R_r,G_g,B_b))$, $\mu g_e(S(R_r,G_g,B_b))$ represents the simultaneous sharpening functions that be expressed as,

$$g_{FBD}(S(R_r, G_g, B_b)) = c_{FBD}(\|\nabla S(R_r, G_g, B_b)\|)\mathrm{div}(\frac{\nabla S(R_r, G_g, B_b)}{\|\nabla S(R_r, G_g, B_b)\|}) \quad (18)$$

The enhancement form of the PDE can be represented as,

$$g_{FBD}(E(R_r,G_g,B_b))=f(g_{FBD}(E(I,m))-(E(R_r,G_g,B_b))) \quad (19)$$

3D reconstruction

Many medical images get scanned, but the reconstruction required considerable time and made the algorithm complicated. Reliable patient details were a fundamental prerequisite for the meaningful preparation of surgical procedures. These models have been recovered from topographic slice stacks. Until starting the 3D conversion process, images was converted from JPEG to DICOM format. Because of the functional reconstruction, three-dimensional osteotomy preparations were based on the 3D paradigm for osteotomies and subsequent relocations of pelvic bone parts. The bone tissue interface links bone relocations with the soft tissue around which the amount of hard tissue and air determined. A soft tissue volumetric representation was required for an effective 3D simulation of soft tissue deformation and for a preoperative study of aesthetic recovery. For better performance, the smart restorative frustum model was used. **Figure 2** shows the step-by-step protocol for using the smart restorative frustum model (SRFM). Three-dimensional (3D) displays provided the depth detail that was inaccessible in 2D content. The binocular difference of the depth cue was added to digital images viewed by the face during 2D-to-3D transfer, significantly enhancing the immersive effect if achieved correctly. The method of calculating the image depths used the values of contrast and accuracy. In the proximity of objects, there was more contrast and sharpness than the farther distant objects. There were also a reverse proportion of contrast and sharpness to depth. Adjacent regions had narrow chrominance values, making them comparable in depth. Chrominance was a composition measure for the 2D image.

By using edge data, the work described the successful method of 2D to 3D conversion. Remarkably, the edge of an item was likely to be the edge of the map. The relative depth value of each area was assigned until the pixels get clustered together. The dissatisfaction paradigm, which divided the image into various groups. The depth of each segment was then calculated using an initial approxima-

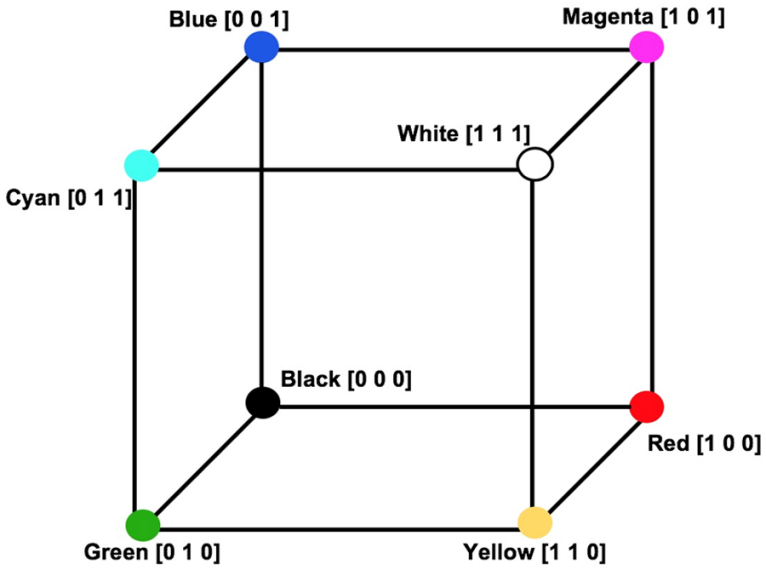

Figure 2. Pixel Color representation.

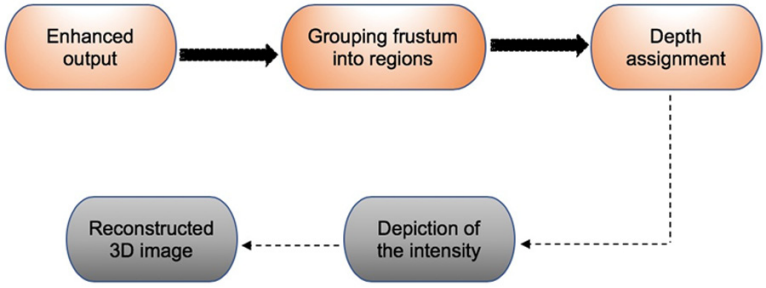

Figure 3. 3D image reconstruction process.

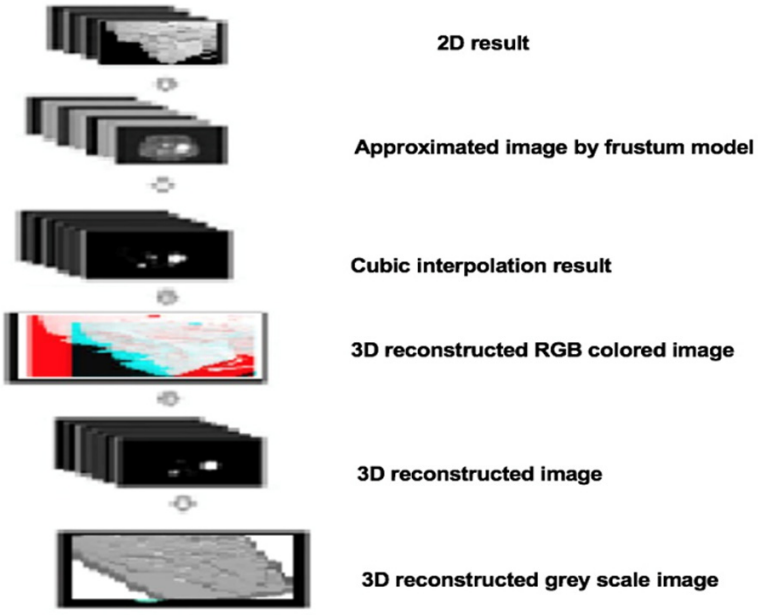

Figure 4. Steps of the reconstruction process.

tion of depth. Finally, the smart restorative frustum model generated a variety of image views. It improved image quality by converting the 2-dimensional image into a comfortable 3-dimensional image without artefacts.

The creation of the 3D image is depicted in **Figure 3**. Both approximate depth and computational complexities was favorably compared by the algorithm suggested. It signified that every pixel in a frustum has the same depth value. Here, the image was differentiated by using the frustum model. The absolute mean difference of the adjacent frustum was used to compute the value of each link between the frustum.

$$Diff(n, d) = |Mean(n) - Mean(d)| \quad (20)$$

Where n and d represented two neighboring frustum blocks. A smaller value indicated that the two frustum blocks looked more similar. The absolute difference between the frustum block averages was determined. By removing the connections of more substantial edges, numerous grouped regions of the frustum were generated. Many small groups were generated, and there was no consistency between the frustum and connectivity. It preserved connectivity and also provided a better spatial result. The effective connection successfully avoided the image's property. The process was then progress to deep extraction, and it was crucial in the conversion process. The main distinction was the understanding of 2-dimensional and 3-dimensional distance. We provided a firm basis for

Table 1. Performance analysis of the suggested methodology over CQ500 dataset

No.	Image	(deep spatial Multiband VGG NET CNN) Proposed		
		Sensitivity	Specificity	Accuracy
1	HG01	98.84	100	99.25
2	HG02	100	98.84	99.12
3	HG03	96.78	97.84	96.87
4	HG04	98.45	98.98	98.32
5	HG05	99.21	99.75	99.42
6	HG06	95.84	98.86	96.78
7	HG07	98.95	98.47	98.17
8	HG08	98.75	99.21	98.79
9	HG09	98.74	98.74	97.86
10	HG10	78.65	96.54	93.78
11	HG11	100	100	100
12	HG12	89.24	95.78	95.87
13	HG13	97.48	97.12	98.47
14	HG14	100	98.02	98.78
15	HG15	100	100	100
16	HG22	97.14	97.15	92.98
17	HG24	100	97.14	94.41
18	HG25	100	98.65	94.05
19	HG26	99.27	99.25	93.65
20	HG27	94.35	97.25	96.78
21	HG28	97.84	98.65	95.16
22	HG29	100	100	90
23	HG30	100	98.58	99.34
24	HG31	100	99.25	93.12
25	HG32	100	99.88	93.76
26	HG33	100	99.45	93.46
27	HG34	100	99.32	99.47
28	HG35	100	98.78	99.06
29	HG36	100	98.45	99.15
30	HG37	99.84	99.89	93.45
Average		99.91233333	99.828	93.7733333

the refinement and enhancement of 3D images by collecting and integrating these depth pixels. After generating the frustum block classes, the required depth for each unit was allocated using the expected depth gradient. Forming gradient plans, assigning depth gradients, and ensuring the accuracy of the recognized field was all part of the procedure.

$$Depth = \sum_{Pixel(x,y)} [W_{frustum(1)}{}^{x-\frac{width}{2}}/_{width} + W_{frustum(2)}{}^{x-\frac{height}{2}}/_{height}] / \text{Pixel number (n)} \quad (21)$$

Greater depth indicated the proximity of the pixel. Each block group had a depth function corresponding to the same degree as the block unit gravity center, as shown by this formula. The meaning of $W_{frustum(1)}$ and $W_{frustum(2)}$ sign was balanced for the slope weight from left to right and from top to bottom. It enabled the depth chart to be developed. Since a bilateral cross-filter provided a continuous depth map with equivalent pixel values throughout the smooth region, the depth map's graphical characteristics was convenient. Finally, the depth map was created. A smooth depth map with equal pixel values within a soft area retains sharp discontinuity and comfortable visual consistency at the object boundary. With three-dimensional projection depth picture processing, the depth map was used to create right or left multi-visual images. Eventually, a pixel to the right or the left of the intermediate point was identified for the 3D view. The location of the pixel is adjusted by depth quality. This formula can recreate the 3D image, through cubic interpolation,

$$x_i{}^3{}_1 = x_a + \left[\frac{t_x}{2} * \frac{f}{z}\right]\hat{}3 \quad (22)$$

The x_i is the horizontal coordinate of the frustum pixel view, f is focal length, t_x is the width, and Z is the actual pixel depth value. The formula indicates the 3D image reconstruction of the intermediate view pixel horizontally the left and the right view.

After then, we measured the object area of each slice. A smart restorative frustum model that can reconstruct the image in a 3D form gives clear visualization of the abnormality.

In **Figure 4**, the preoperative 3D image was created from a 2D image after following the multiple steps.

Face prediction

The technique of choice for complex craniomaxillofacial dysplasia is a 3D analysis that focuses on topographical details and virtual patterns. A cephalometric and functional exam may distinguish facial areas that differ or indi-

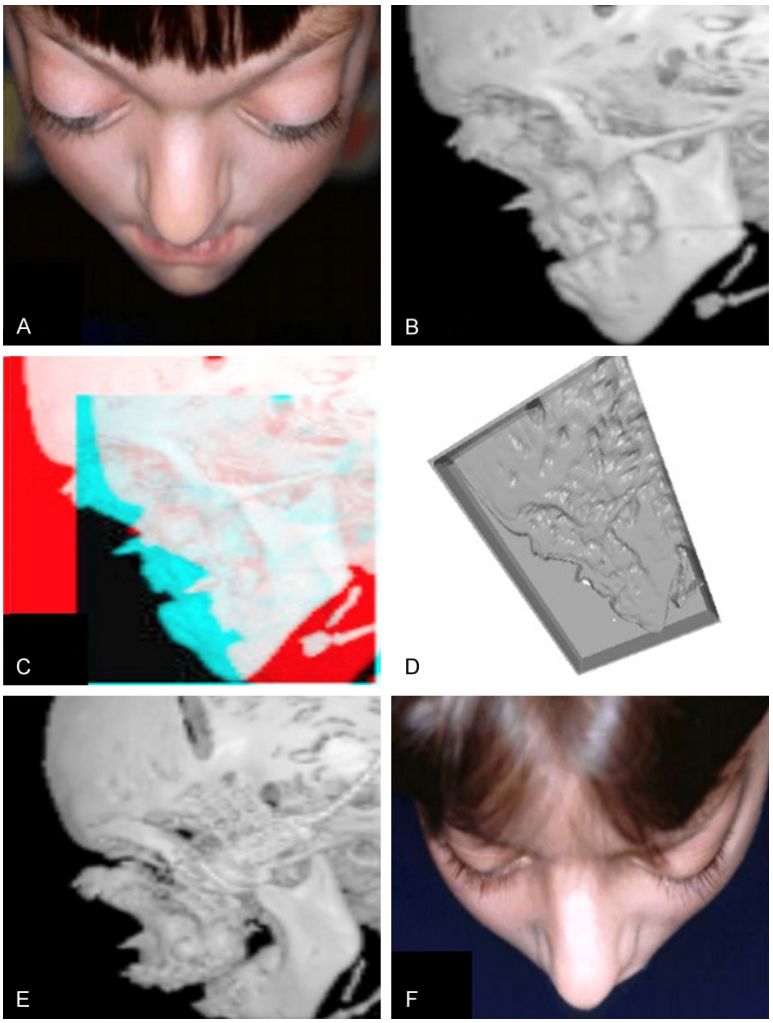

Figure 5. Image reconstruction and post-operative face representation. Preoperative face (A), 2D image (B), 3D reconstructed RGB colored image (C), 3D reconstructed grey scale image (D), estimated postoperative image (E) and postoperative image (F).

cate functional failure from bilateral symmetry. Facial dysplasia correction usually means that the face structure is moved, removed, increased, or even replaced entirely. As a result, bone must be replaced, and an operation must be carefully planned. The osteotomies were designed in complex cases with skull replicas of life-size. Moving bone sections was rearranged to maintain anatomical symmetry and to restore functional anatomy. The comparison of different concepts of care includes a variety of policy models. This approach is not necessarily viable when health care rates rise, and public health insurance costs fall. Our objective was to create an immersive computing environment that allows the operator to anticipate complex osteotomies and bone transfers using simulated models. Different methods are then practically free to search. The planning of computer-assisted osteotomy was based on the above definition. The deep spatial multiband VGG NET CNN can be refined as neural and has multiple hidden nonlinear layers. It is pre-trained in the nonlinear dimension reduction of the data, and the network model can provide additional sensory feedback. The face region here needed to be distinguished and dismantled. The classification system was used to classify facial images by various features to improve the form and face recovery process. The proposed classification was used for improvement or specific functionality to extract the non-linear properties of facial images. The use of classification techniques showed the face images with existing accuracy, efficiency, and continuity. The featured photos identified the need for facial reconstruction. The classification system was based on the derived characteristics. The classifier was likely to calculate and perform a function. The data was first analyzed and resized in the whole system by classification and then measured by class probability; the method was used preoperatively. By giving different input parameters, the suggested classifier predicted the facial structure. Post-operative face according to the rating model was expected. Finally, a ranking was generated for the matching distance of data.

$$obj_{ED} = -20 * q(-2 * \sqrt{\sum S_v})/2 - \exp(\sum \cos(2\pi * S_v)/d_b) + 20\exp \quad (23)$$

Where ED signifies the Euclidean distance, q denotes the query data, and s is the score value of the image.

$$\text{classify } F(obj_{ED}) = a_j^{\prime} b_j^{\prime} \quad (24)$$

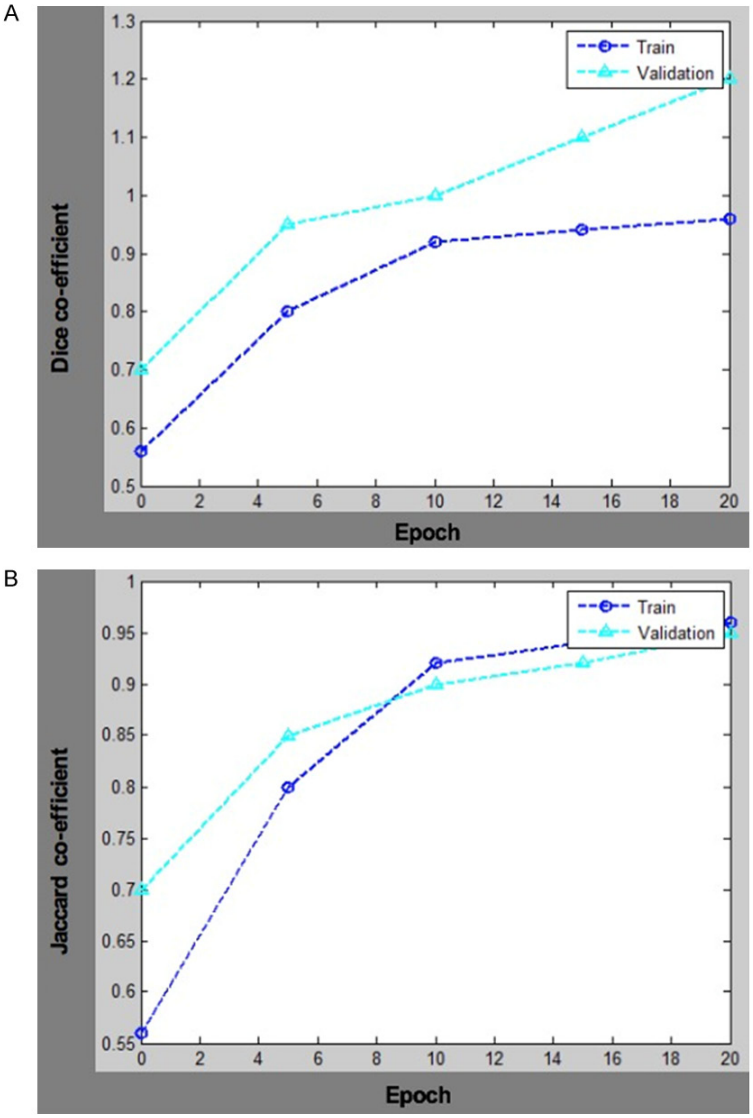

Figure 6. Dice (A) and Jaccard co-efficient (B).

The classification concluded as,

$$F = a_j^l b_j^l - n(a_j^l b_j^l)^2 \quad (25)$$

Where F denotes the feature, P represents the pointed feature, $a_j^l b_j^l$ are the classified features.

Algorithm 1: (deep spatial Multiband VGG NET CNN)

Input: Enhancement image e_{im}

Output: Post-operative face image F_c

Initialize the classifier layers

Initialize the vgg layers

Integrate vgg layers

Initialize train attributes

Set label

Train label =80%

Tet label =20%

Lab = unique (label)

For ii =1: lengh (Lab)

Class = find (label == Lab (ii))

To pass train attributes data to each layer,

Train cut = length (class)-train cut

Traindata = [train data; train attributes; class (1: Traincut) end-5: end]

Predict label = classify (net, train data)

End

End

For ii =1: size (train data, 1)

Traindata = [train data; train attributes; class (1: Traincut) end-5: end]

End

For ii =1: size (train attributes, 1)

Test data = [train attribute; class (1: Train cut) end-5: end]

End

Result and discussion

The computer-assisted modeling, planning, and simulation method enables the preoperative evaluation based on of 3-D simulations with various therapeutic strategies. The anatomical and functional limits of bone structures may be mobilized and moved. With high-quality

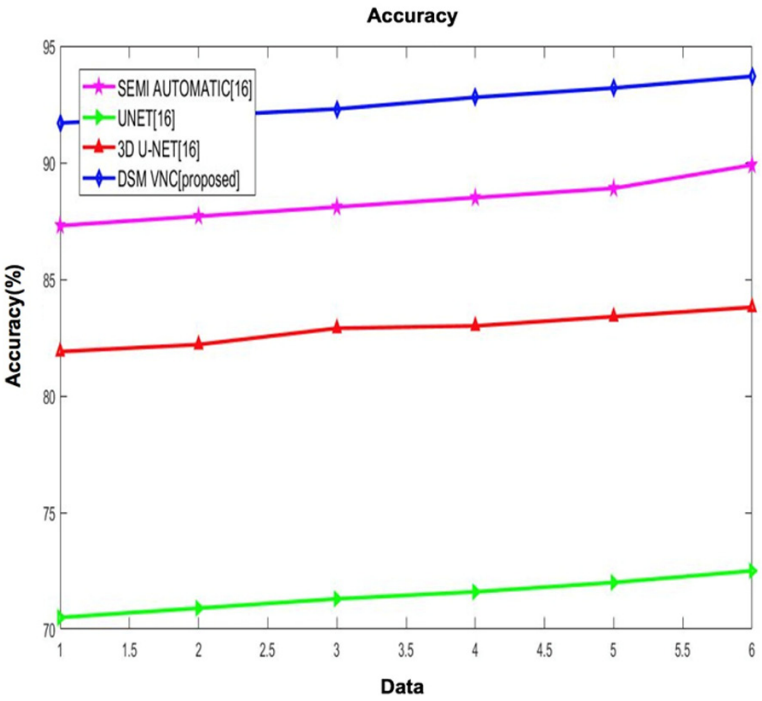

Figure 7. Determination of the accuracy percentile.

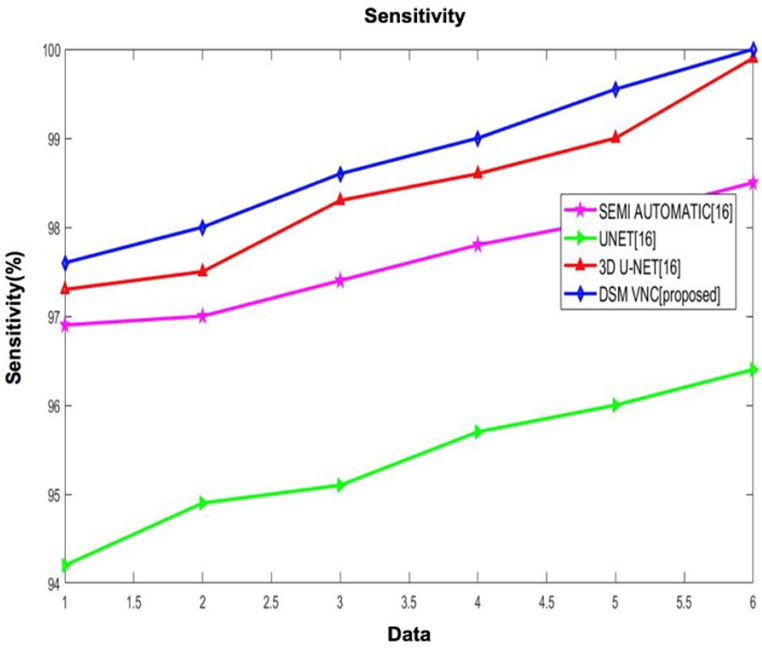

Figure 8. Data vs. sensitivity (%).

modeling methods, the resultant facial expression is simulated and visualized. This method is essential for preoperative surgical preparation and for keeping active patient records, documentation, quality control, and surgical training. **Table 1** shows the average forecast performance. After preprocessing and enhancement stage, image slices in which the post-operative face can be predicted by using a deep spatial Multiband VGG NET CNN classifier. The following **Figure 1** shows the output of the suggested classifier. It can be noted from the dataset of identified post-operative faces. For the output of the proposed work, MATLAB was used. This section has analyzed the efficiency of the proposed method.

Dataset

We collected the 313,318 head CT scan dataset and its clinical records from different centers. Of these, the algorithms were developed by 21,095 scans (Qure25k data set). In addition, CQ500 datasets from various centers were compiled in two batches, B1 and B2, to verify the algorithms clinically. 491 scans used the CQ500 dataset. Three independent radiologists agreed with the standard for CQ500 results, while the gold standard for Qure-25k data collection is called the clinical report (http://headctstudy.qure.ai/#dataset). All data mentioned above are open-source; hence, no approval for ethical committee was required.

Figure 5A-F, initially reconstructed the input image, and then the post-operative face was designed. The suggested deep spatial Multiband VGG NET CNN has shown a high accuracy range over post-operative face prediction, and the measuring precision reveals the tool's actual mass and efficiency. Therefore, successful metrics such as the Jaccard and Dice scores

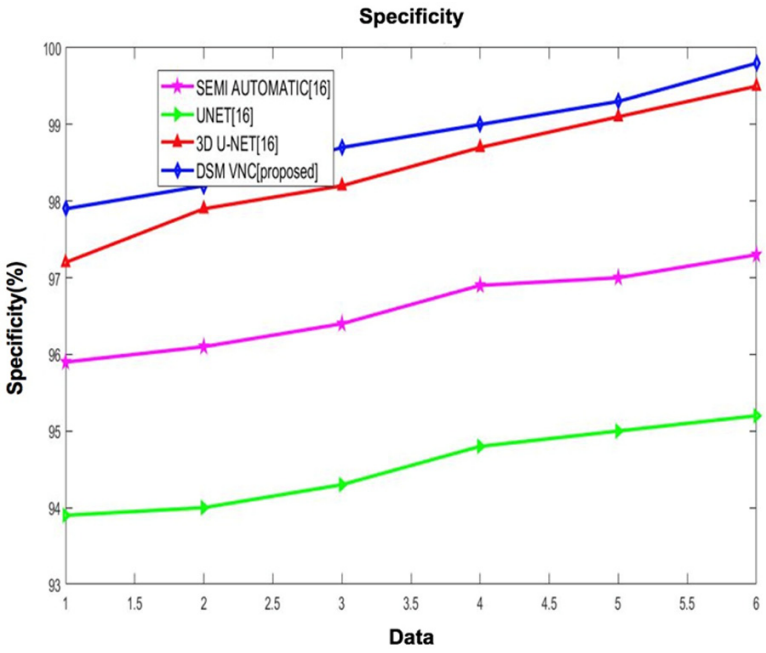

Figure 9. Data vs. specificity (%).

have shown accurate outcomes compared to other traditional methods.

Dice co-efficient

Let C and D be the pixels for the ground truth and the pixels marked. They can then determine the coefficient as the dice.

$$I(A, B) = (2\ A \cap B/A+B) = 2TP/2TP+FN+FP \quad (26)$$

Jaccard co-efficient

The similarity between the diverse communities can be established.

$$J(A, B) = (A \cap B/A \cup B) = (A \cap B)/A+B - (A \cap B) = (TP/TP+FN+FP) \quad (27)$$

The Dice and Jaccard scores for the suggested deep spatial VGG NET CNN solution is seen in **Figure 6A**, **6B**. The findings demonstrated that the recommended procedure displays accurate high Jaccard and Dice coefficient values. It can compare with the other existing methods to prove the efficiency of the proposed model as shown in reference [22].

The proposed classification system exceled the existing approaches with a maximum accuracy yield of 93.7 percent, presented in **Figure 7**. It is evident from the obtained findings that the proposed approach is way above the current methods.

Figure 8 depicts the suggested system, which shows higher sensitivity rates (99.9%) than the current method.

Figure 9 compares the accuracy of the specificity values achieved by the proposed system with the current methods. The findings clearly show that the proposed approach has provided a high specificity rate (99.8%) relative to the previous approaches. The results indicate that the proposed method can achieve the desired performance.

Conclusion

Through this study, the estimation of the post-operative face based on the new approach remains the most complicated issue in the medical sector. By utilizing the visual skull CT representations, the current procedure effectively identifies the post-operative face. This research aims to effectively and efficiently recognize the post-operative face and save time and resources. This method contrasts with the three others recently introduced approaches to evaluate the system's efficiency. Compared to different current methods, the output of the suggested protocol indicates positive effects. In the future, we will try to implement the recommended procedure for disease diagnosis.

Acknowledgements

This study was supported by the National Natural Science Foundation of China (No. 81873937).

Disclosure of conflict of interest

None.

Address correspondence to: Dr. Jinghong Xu, Department of Plastic Surgery, The First Affiliated Hospital, School of Medicine, Zhejiang University, No. 79 Qingchun Road, Hangzhou 310003, China. Tel: +86-571-87236307; E-mail: 1304017@zju.edu.cn

References

[1] Kanevsky J, Corban J, Gaster R, Kanevsky A, Lin S and Gilardino M. Big data and machine learning in plastic surgery: a new frontier in surgical innovation. Plast Reconstr Surg 2016; 137: 890e-897e.

[2] Schmelzeisen R, Schön R, Schramm A and Gellrich NC. Computer-aided procedures in implantology, distraction and cranio-maxillofacial surgery. Ann R Australas Coll Dent Surg 2002; 16: 46-49.

[3] Shahim K, Jürgens P, Cattin PC, Nolte LP and Reyes M. Prediction of cranio-maxillofacial surgical planning using an inverse soft tissue modelling approach. Med Image Comput Comput Assist Interv 2013; 16: 18-25.

[4] Okamoto D, Yamauchi K, Yazaki M, Saito S, Suzuki H, Nogami S and Takahashi T. A comparison of postoperative, three-dimensional soft tissue changes in patients with skeletal class III malocclusions treated via orthodontics-first and surgery-first approaches. J Craniomaxillofac Surg 2021; 49: 898-904.

[5] Bianchi A, Muyldermans L, Di Martino M, Lancellotti L, Amadori S, Sarti A and Marchetti C. Facial soft tissue esthetic predictions: validation in craniomaxillofacial surgery with cone beam computed tomography data. J Oral Maxillofac Surg 2010; 68: 1471-1479.

[6] Gateno J, Xia J, Teichgraeber JF and Rosen A. A new technique for the creation of a computerized composite skull model. J Oral Maxillofac Surg 2003; 61: 222-227.

[7] Uechi J, Okayama M, Shibata T, Muguruma T, Hayashi K, Endo K and Mizoguchi I. A novel method for the 3-dimensional simulation of orthognathic surgery by using a multimodal image-fusion technique. Am J Orthod Dentofacial Orthop 2006; 130: 786-798.

[8] Nairn NJ, Ayoub AF, Barbenel J, Moos K, Naudi K, Ju X and Khambay BS. Digital replacement of the distorted dentition acquired by cone beam computed tomography (CBCT): a pilot study. Int J Oral Maxillofac Surg 2013; 42: 1488-1493.

[9] Steinbacher DM. Three-dimensional analysis and surgical planning in craniomaxillofacial surgery. J Oral Maxillofac Surg 2015; 73: S40-56.

[10] Bauermeister AJ, Zuriarrain A and Newman MI. Three-dimensional printing in plastic and reconstructive surgery: a systematic review. Ann Plast Surg 2016; 77: 569-576.

[11] Bhalodia R, Dvoracek LA, Ayyash AM, Kavan L, Whitaker R and Goldstein JA. Quantifying the severity of metopic craniosynostosis: a pilot study application of machine learning in craniofacial surgery. J Craniofac Surg 2020; 31: 697-701.

[12] Jalali A, Lonsdale H, Zamora LV, Ahumada L, Nguyen ATH, Rehman M, Fackler J, Stricker PA and Fernandez AM. Machine learning applied to registry data: development of a patient-specific prediction model for blood transfusion requirements during craniofacial surgery using the pediatric craniofacial perioperative registry dataset. Anesth Analg 2021; 132: 160-171.

[13] Brucoli M, Boffano P, Franchi S, Pezzana A, Baragiotta N and Benech A. The use of teleradiology for triaging of maxillofacial trauma. J Craniomaxillofac Surg 2019; 47: 1535-1541.

[14] van de Lande LS, Papaioannou A and Dunaway DJ. Geometric morphometrics aided by machine learning in craniofacial surgery. J Orthod 2019; 46: 81-83.

[15] Miller MQ, Hadlock TA, Fortier E and Guarin DL. The auto-eFACE: machine learning-enhanced program yields automated facial palsy assessment tool. Plast Reconstr Surg 2021; 147: 467-474.

[16] Tonutti M, Gras G and Yang GZ. A machine learning approach for real-time modelling of tissue deformation in image-guided neurosurgery. Artif Intell Med 2017; 80: 39-47.

[17] Stepanek L, Kasal P and Mestak J. Evaluation of facial attractiveness for purposes of plastic surgery using machine-learning methods and image analysis. 2018 IEEE 20th International Conference on e-Health Networking, Applications and Services (Healthcom). IEEE 2018; 1-6.

[18] Mostoufi B and Caccamese JF. Computer-assisted orthognathic surgery from prediction to navigation. In: Keyhan SO, Fattahi T, Bagheri SC, Bohluli B, Amirzade-Iranaq MH, editors. Integrated procedures in facial cosmetic surgery. Cham: Springer International Publishing; 2021. pp. 703-726.

[19] Gerbino G, Autorino U, Borbon C, Marcolin F, Olivetti E, Vezzetti E and Zavattero E. Malar augmentation with zygomatic osteotomy in orthognatic surgery: bone and soft tissue changes threedimensional evaluation. J Craniomaxillofac Surg 2021; 49: 223-230.

[20] Van Hemelen G, Van Genechten M, Renier L, Desmedt M, Verbruggen E and Nadjmi N. Three-dimensional virtual planning in orthognathic surgery enhances the accuracy of soft tissue prediction. J Craniomaxillofac Surg 2015; 43: 918-925.

[21] Hertanto M, Ayoub AF, Benington PCM, Naudi KB and McKenzie PS. Orthognathic patient perception of 3D facial soft tissue prediction planning. J Craniomaxillofac Surg 2021; 49: 783-788.

[22] Fauser J, Stenin I, Bauer M, Hsu WH, Kristin J, Klenzner T, Schipper J and Mukhopadhyay A. Toward an automatic preoperative pipeline for image-guided temporal bone surgery. Int J Comput Assist Radiol Surg 2019; 14: 967-976.